

# Novel Method for Background Phase Removal on MRI Proton Resonance Frequency Measurements

Wolfgang Stefan<sup>1,3</sup>, David Fuentes<sup>1</sup>, Erol Yeniaraş<sup>2</sup>, Ken-Pin Hwang<sup>1</sup>,  
John D. Hazle<sup>1</sup>, and R. Jason Stafford<sup>1</sup>

<sup>1</sup>*Departments of Imaging Physics, The University of Texas MD Anderson Cancer Center, Houston,  
Texas, 77054*

<sup>2</sup>*erol.yeniaraş@gmail.com*

<sup>3</sup>*Corresponding author: wstefan@mdanderson.org*

November 12, 2021

## 1 Introduction

Phase data provides information for a variety of applications in magnetic resonance imaging (MRI) including shimming, artifact removal, temperature imaging, and improving soft tissue contrast [1, 2, 3, 4, 5]. One of the most prominent examples of using phase images as an additional contrast mechanism is susceptibility weighted imaging (SWI), which is useful in a wide variety of neuro-pathologies, e.g., traumatic brain injury, cerebral microhemorrhages, cerebrovascular disease, multiple sclerosis, intracranial hemorrhage, and tumors [6, 7]. Quantitative susceptibility mapping is another useful application of using phase images to complement magnitude data [8, 9]. The MR phase data is directly related to the proton resonance frequency (PRF) when gradient echo imaging sequences are used. In order to make best use of phase data it is necessary to accurately separate the background phase (e.g., generated by local field inhomogeneities, air-tissue interfaces, etc.) from the phase contributions of tissue magnetic susceptibility differences.

Reference scans, in which an identical object is scanned with the susceptibility sources removed, provides the most reliable background field measurements [8, 10].

However, it is impractical or impossible to perform a reference scan in many *in vivo* situations.

The background can be estimated and removed, if *a priori* knowledge of the spatial distribution of all background susceptibility sources [11, 12] can be assumed. The assumption of the separability between local and background fields in a certain space is often violated, leading to erroneous estimation of local fields, and the results depend on the choice of the basis functions [13]. In practice, the knowledge of the background susceptibility source surrounding a given region of interest (ROI) is often not fully available or sufficiently accurate. This leads to substantial residual background field that requires additional attention, particularly when there are significant variations in susceptibility outside the imaging field of view (FOV) [11].

Current background removal techniques, that do not require prior knowledge of the background susceptibility source assume that the local and background fields are in a space spanned by the Fourier basis [14] or polynomial functions are separable [8, 13, 15]. Usually, a user defined (or

automatically determined) ROI has to be defined. In [16] the selection of the ROI for the polynomial interpolation problem is avoided using a reweighted  $\ell_1$  regression.

Another method to estimate the background is to solve a Dirchlet boundary problem of the Laplace or Poisson equation [17, 9, 18]. It is argued in [17] that the Laplace solution is potentially more stable than polynomial interpolation and provides physically more meaningful solutions because the magnetic field and thus the PRF in homogeneous tissue has the property  $\nabla^2\Phi = 0$ . However this method also relies on the manual selection of an ROI.

In this paper, we seek to remove the background without the use of a reference PRF map, an ROI or an heuristic basis like the Fourier or polynomials. It can be interpreted as physically meaningful similar to the arguments in [17, 9], and has very limited computational costs. On the basis of its smoothness, the proposed method suppresses the background, rather than estimating and subtracting it. We assume that sharp changes in the image are either due to tissue-tissue interfaces or due to the heating, while the background is smooth (i.e., does not contain very large gradients). We also assume that sharp gradients are sparse, i.e., only a few pixels contain either tissue-tissue interfaces or heating, and that the PRF for the rest of the image is a harmonic function. Our background suppression algorithm has two stages; First sharp gradients are detected in the phase image, using a sparsity enforcing edge detection method. Second a corrected PRF map is found, which has the same sharp gradients, and satisfies  $\nabla^2\Phi = 0$  in the smooth regions. As a consequence the difference between the original PRF map and the corrected PRF map is a harmonic function, which is physically meaningful as argued in [17, 9].

Our approach can be used in 2D and 3D. Practically, temperature measurements are performed on 2D scans because of time constraints. In this case we make the approximation, that the background is harmonic w.r.t. the partial derivatives in the imaging plane.

## 2 Algorithm

For the following discussion all functions defined on a continuous domain are non-bold letters while discretely defined functions are denoted as bold letters. The bold letter variables can always be interpreted as vectors by reordering.

The phase,  $\Phi(x, y)$ , of the measured MRI signal at position  $(x, y)$  is modeled as a function defined on a continuous domain

$$\Phi(x, y) = \Phi_b(x, y) + \Phi_h(x, y),$$

where  $\Phi_h(x, y) \in (-\pi; \pi]$  is the phase change due to structures of interest (e.g., heating or susceptibility differences) and  $\Phi_b(x, y) \in (-\pi; \pi]$  is the background phase due to  $B_0$  field inhomogeneities. Practically we are limited to pixel or voxel based evaluations of  $\Phi$ ,  $\Phi_b$  and  $\Phi_h$ . The underlying continuously defined functions are used to derive the method but usually remain unknown. To separate  $\Phi_b$  and  $\Phi_h$ , a common assumption is that  $\Phi_b$  has slow spatial variations and  $\Phi_h$  has large spatial variations, for example as measured by the magnitude of the gradient. However, it can be difficult to determine if large gradients of  $\Phi$  are due to large variations of  $\Phi_h$  or the background. Thus, a tunable approach is needed to separate the two.

To illustrate the idea behind our approach, assume for simplicity,  $\Phi_h$  is a piecewise constant function. Further, assume that  $\Phi_b$  is a smooth function (i.e., derivatives of any order are bounded). Panel a) of Figure 1 shows an example. Then  $\Phi_b$  can be estimated from  $\Phi$  as illustrated in Panel e): First, find the jump size and direction (up or down) of the discontinuities (Panel c). Because

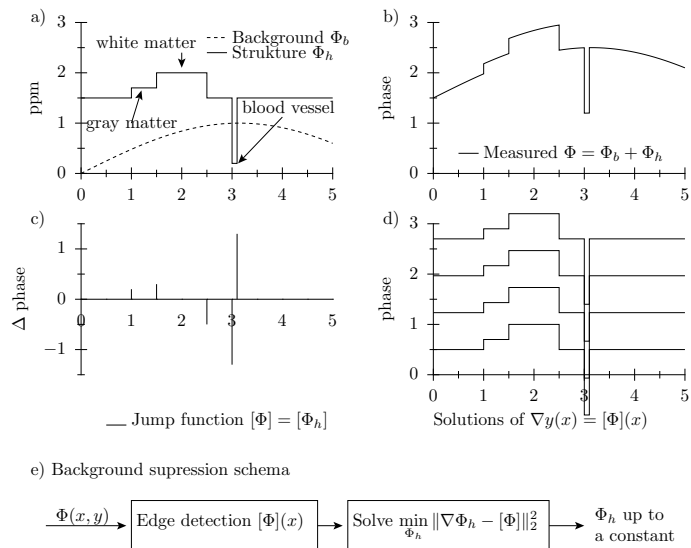


Figure 1: Illustration of the proposed background suppression method. Panel a) shows the desired phase signal due to different structures  $\phi_h$  and the background signal  $\phi_b$ . Panel b) shows the measured signal  $\phi$ . The common jump function (i.e. the height of the jumps) of  $\phi$  and  $\phi_h$  is shown in Panel c). The desired  $\phi_h$  can be obtained from  $[\phi]$  up to a constant as shown in Panel d). Panel e) illustrates the proposed method to recover  $\phi_h$  from  $\phi$ .

$\Phi_b$  is smooth and does not contain jumps, all jumps in  $\Phi$  are due to jumps in  $\Phi_h$ . Further, as a piecewise constant function,  $\Phi_h$  is defined by its jump discontinuities up to an additive constant as illustrated in Panel d). I.e. if we find a function with the same jump discontinuities in size and direction as  $\Phi$  which has zero gradient away from edges, then, this function is equal to  $\Phi_h$  up to an additive constant. This constant can, for example, be determined if we assume that  $\Phi_h$  is zero in a particular region of the image, for example in regions outside of the heating zone. Phase wrapping artifacts can easily be removed if jumps larger or equal to  $2\pi$  are projected back to the interval  $[0, 2\pi)$ .

## 2.1 Edge detection

We limit the description of the algorithm to 2D functions, more dimensions are treated analogous to the 2D case. Two main approaches have been proposed in the literature to detect edges. One approach is to characterize edges in a pixel-based image by identifying regions of sharp variations from differences between neighboring pixels, e.g., the Canny edge detector [19]. Another approach uses a wavelet representation of the image to identify the edges, see e.g., [20]. However, both approaches cannot easily distinguish sharp edges from steep gradients [21], which in our case, leads to an insufficient removal of the background. Additionally,  $\Phi$  does not contain real jump discontinuities because almost all natural images, and the considered MRI phase images in particular, are corrupted by some degree of blurring. Therefore a useful edge detection for this application has to allow sharp gradients to be identified as edges, while dismissing less sharp gradients as background. Here, we propose a method that includes a tuning parameter to achieve an appropriate separation

of background phase and phase of interest.

The tuning parameter has to be chosen on a case to case basis by visually inspecting the images. We have found that for similar applications, such as removing the background field in brain MRI scans, similar parameters can be used.

To make the edge detection more robust, we assume only very few pixels contain sharp gradients, i.e. the gradients are *sparse*. This assumption is similar to the sparsity assumption that is usually made in a compressed sensing approach [22]. Therefore, we choose the approach in [23] which is sparsity enforcing and robust in the presence of steep gradients. The proposed method is similar to the method described in [23], with the difference, that we exchange the edge detection kernels that are based on partial Fourier from the original publication with a kernel based on finite differences as described as follows.

Analogous to [24], edges in  $\Phi(x, y)$  are represented by the so called *jump functions* in  $x$ - and  $y$ -direction denoted by  $[\Phi]_x(x, y)$  and  $[\Phi]_y(x, y)$ . The jump functions are defined by

$$\begin{aligned} [\Phi]_x(x, y) &= \Phi(x^+, y) - \Phi(x^-, y) \\ [\Phi]_y(x, y) &= \Phi(x, y^+) - \Phi(x, y^-) \end{aligned}$$

where  $x^+$ ,  $y^+$ ,  $x^-$  and  $y^-$  are the well defined right and left hand limits. If  $\Phi(x, y)$  is smooth with respect to  $x$  and  $y$  at  $(x, y)$ , then  $[\Phi]_{\{x, y\}}(x, y) = 0$ . Further,  $[\Phi]_x(\xi, \nu)$  or  $[\Phi]_y(\xi, \nu)$  is the height of the jump if  $\Phi$  has a jump in  $x$ - or  $y$ -direction at  $(\xi, \nu)$  respectively. Our goal is to find discrete representations of the jump functions.

Assume a pixelated image is given by sampling a function defined on a continuous domain on a regular grid, i.e.,  $(\Phi)_{i, j} = \Phi(x_i, y_j)$ , where  $i, j = 1, \dots, N$ . Since the underlying continuously defined function  $\Phi$  is not known, finding an approximate for reliable edge detection is very difficult. In [24, 21] the underlying function is expressed as a Taylor expansion around a given pixel location. The remainder of a Taylor expansion up to degree  $m$ , vanishes if the underlying function is a polynomial of degree  $m$  in the neighborhood of the given pixel. Similarly, if the underlying function is not a polynomial, but is sufficiently smooth, i.e., has several continuous derivatives, the remainder can be expected to be very small. On the other hand, it is very large at the locations of jump discontinuities. If the Taylor expansion is approximated by the interpolating polynomial around a given grid point, this idea leads to the so called *polynomial annihilation* edge detection method, described in [24], which can be expressed as

$$\begin{aligned} (\mathbf{g}_x^m)_{i, j} &= \sum_{k=1}^{m+1} c_{m, k} \Phi(x_{i+k}, y_j) \\ (\mathbf{g}_y^m)_{i, j} &= \sum_{k=1}^{m+1} c_{m, k} \Phi(x_i, y_{j+k}) \end{aligned} \tag{1}$$

where  $\mathbf{g}_x^m$  and  $\mathbf{g}_y^m$  are the jump function approximations for a  $m^{\text{th}}$  order polynomial edge detector, and

$$c_{m, k} = -\frac{m!q_m}{\prod_{l=1, k \neq l}^{m+1} (k-l)}. \tag{2}$$

The scalars  $q_m$  is chosen such that the jump height is preserved. A more detailed discussion and derivation of the edge detection kernels  $c_{m, k}$  can be found in [25]. From here on we fix the order  $m$ , if not indicated otherwise, and drop it from  $\mathbf{g}$  and  $\mathbf{c}$  for clarity. The sums in (1) can be computed

by a convolution:

$$\begin{aligned}\mathbf{g}_x &= \mathbf{c} * \Phi \\ \mathbf{g}_y &= \mathbf{c}^T * \Phi,\end{aligned}\tag{3}$$

where  $\mathbf{c}$  is obtained from (2) by zero padding:

$$\mathbf{c}_{i,k} = \begin{cases} c_{m,k} & \text{for } i = 1 \text{ and } k \leq m + 1 \\ 0 & \text{otherwise} \end{cases},\tag{4}$$

and  $\mathbf{c}_{i,j}^T = \mathbf{c}_{j,i}$ .

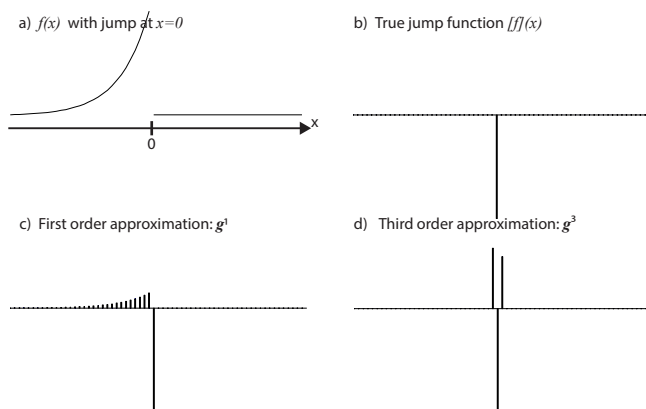


Figure 2: Illustration of the jump function (b) of a piecewise smooth function (a). The approximations using low order (c) and high order (d). Lower order (c) can lead to miss classification of edges in regions of large gradients. Higher order (d) produces unwanted oscillations.

It is shown in [24, 21] that (1) converges to the true jump function as  $N \rightarrow \infty$ , however, this method introduces oscillations near locations of edges. These oscillations can easily lead to misclassification of edges. Figure 2 shows a test function  $f(x)$  in panel a and its true jump function  $[f](x)$  in panel (b). Panel (c) shows the discrete approximation of the jump function using  $m = 1$  ( $\mathbf{g}^1$ ). The non-zero components of the jump function approximation can easily be misinterpreted as edges. Panel (d) shows the discrete approximation of the jump function using  $m = 3$  ( $\mathbf{g}^3$ ). The oscillations around the jump are artifacts of the higher order method.

To reduce the oscillations a non-linear filtering technique has been used which combines the jump function approximations of several orders to one combined jump function. However this approximation is very sensitive to noise [24, 21]. In [23] it was proposed to remove similar oscillations by deconvolution. Oscillations are modeled as a Point Spread Function (PSF), the so called *matching waveform*, and removed using  $\ell_1$  minimization, which forces the edges to be sparse. In [23] a closed form solution of the matching waveform is used to perform the deconvolution. Because the matching waveform based on (1) has no closed form it has to be estimated. An estimate can be obtained by applying (1) to a unit jump, i.e. a jump in either  $x-$  or  $y-$  direction with size one. This results in

the matching wave form

$$\mathbf{w}_{i,j} = \begin{cases} \sum_{k=1}^{N/2} \mathbf{c}_{k,j} + \sum_{k=N-i+2}^N \mathbf{c}_{k,j} & i = 1, \dots, N/2 \\ \sum_{k=N-i+2}^{N/2} \mathbf{c}_{k,j} & i = N/2 + 1, \dots, N \end{cases}, \quad (5)$$

for edge detection kernels of order  $m$ .

Let  $\mathbf{u}_x$  be the true jump function in  $x$ - direction, and  $\mathbf{u}_y$  be the true jump function in  $y$ - direction. Given the matching wave form  $w$  we assume  $\mathbf{g}_x \approx \mathbf{w} * \mathbf{u}_x$  and  $\mathbf{g}_y \approx \mathbf{w}^T * \mathbf{u}_y$ , where  $\mathbf{u}_x$  and  $\mathbf{u}_y$  are the desired jump function approximations. Thus, using (3), approximations of  $\mathbf{u}_x$  and  $\mathbf{u}_y$  can be found by solving the optimization problem

$$\begin{aligned} (\mathbf{u}_x, \mathbf{u}_y) = \arg \min_{(\mathbf{u}_x, \mathbf{u}_y)} & \frac{1}{2} \|\mathbf{w} * \mathbf{u}_x - \mathbf{c} * \Phi\|_2^2 \\ & + \frac{1}{2} \|\mathbf{w}^T * \mathbf{u}_y - \mathbf{c}^T * \Phi\|_2^2 \\ & + \lambda (\|(\mathbf{u}_x, \mathbf{u}_y)\|_{1,2}), \end{aligned} \quad (6)$$

where  $\|(\mathbf{u}_x, \mathbf{u}_y)\|_{1,2} = \sum_{i,j} \sqrt{((\mathbf{u}_x)_{i,j})^2 + ((\mathbf{u}_y)_{i,j})^2}$  and  $\lambda$  is a regularization parameter. In the appendix a proof of convergence of the proposed method to the true jump function as  $N \rightarrow \infty$  similar to the results in [24, 21] is presented.

The measured phase  $\Phi$  contains jump discontinuities of size  $2\pi$  due to phase wrapping. With the assumption that there are no jumps larger than  $2\pi$  due to structure, it is easy to identify jumps from phase wrapping. To remove all jumps from phase wrapping we replace  $\mathbf{u}_x \rightarrow (\mathbf{u}_x \bmod 2\pi)$  and  $\mathbf{u}_y \rightarrow (\mathbf{u}_y \bmod 2\pi)$ . To solve the optimization problem an augmented Lagrangian method can be used, e.g., see [26].

## 2.2 Phase image reconstruction

In the second stage a convex optimization problem is solved to find a function such that its gradients match the detected sharp gradients of the phase.

$$\min_{\Phi_h} \|\nabla \Phi_h - (\mathbf{u}_x, \mathbf{u}_y)\|_{\mathbf{m}}^2 + \epsilon \|\Phi_h\|_2^2, \quad (7)$$

where

$$\|\xi\|_{\mathbf{m}}^2 = \sum_{i,j} \mathbf{m}_{i,j} |\xi_{i,j}|^2,$$

and  $\mathbf{m}$  is chosen such that unreliable phase measurements are down-weighted. We use the square of the magnitude of the image as weights because it has previously been connected to noise in the phase [27]. The second part of (7) is needed (i.e.,  $\epsilon > 0$ ) because  $\nabla \Phi_h$  is invariant to an additive constant. We choose  $\epsilon$  large enough to make the problem numerically stable but small enough that the regularization does not change the gradient of the solution significantly ( $\epsilon \approx 10^{-8}$ ).

For a given ROI that does not contain edges, the minimizer of (7) automatically satisfies the Laplace equation  $\vec{\nabla}^2 \Phi_h = 0$ . Note that as a consequence the algorithm separates the phase in a harmonic part (away from edges) and a non-harmonic part at the edges. The background phase can be found by subtracting  $\Phi_h$  from  $\Phi$ .

Because the edges are removed the background  $\Phi_b$  is a continuous function, it is not necessarily harmonic because it may contain discontinuities in higher derivatives. The method could be expanded to detect and remove discontinuities in higher derivatives, see e.g. [28], however the noise content in the images may be a problem since edge detection on gradients are very sensitive to noise.

The background suppression procedure is summarized in Algorithm 1.

---

**Algorithm 1** Background suppression algorithm overview

---

**Require:** A complex MRI image  $\mathbf{f} \in \mathcal{C}^{\text{Npixel}}$

**Ensure:**  $\Phi_h$ .

1. Find sharp gradients  $(\mathbf{u}_x, \mathbf{u}_y, \mathbf{u}_z)$  in the phase of  $\mathbf{f}$  using sparsity enforcing edge detection.
  2. Solve  $\min_{\mathbf{x}} \|\nabla \mathbf{x} - (\mathbf{u}_x, \mathbf{u}_y, \mathbf{u}_z)\|_{\mathbf{m}}^2 + \epsilon \|\mathbf{x}\|_2^2$  with weighting  $\mathbf{m} = |\mathbf{f}|^2$
  3. Find  $a \in \mathcal{R}$ , such that  $(\mathbf{x})_{i,j,k} + a = r$  for a reference voxel, i.e.  $r = \Phi_{i,j,k}$
  4.  $\Phi_h := \mathbf{x} + \mathbf{a}$
- 

### 3 Results and Discussion

We apply the proposed method to MR temperature imaging and  $\Phi_b$  correction of PRF measurements.

#### 3.1 Reference-less temperature imaging

For temperature imaging, complex valued 2D images are collected using a gradient echo pulse sequence. Acquisition parameters: Spoiled gradient recalled sequence,  $B_0 = 1.5T$ ,  $TR = 27ms$ ,  $TE = 12ms$ , Pixel Bandwidth  $280Hz$ , Matrix  $256 \times 128$ .

Figure 3(a) and (b) shows the magnitude and phase of the acquired image during a laser induced thermal therapy. The dark regions inside the box cause a signal loss due to the heating. At the corresponding location in the phase image a negative shift of the phase due to the heating can be seen. This shift is linear with temperature change and is used to measure temperature changes. The phase variations outside the heating zone are off resonance effects from an in-homogeneous  $B_0$  field, i.e.  $\Phi_b$ . The jumps (white to black) are due to phase wrapping artifacts. In Panels (c) and (d) two jump function approximations of the phase image computed using (6) with a kernels of order one and three are shown. Similar to the example in Figure 2 the first order jump function approximation is non-zero in areas of large gradients. If the first order approximation is used in (7), then the reconstructed image shows the same background that original phase image has. On the other hand, if the third order approximation is used in (7), then the resulting reconstruction has a suppressed background phase. The parameter  $\lambda$  in (6) is used to suppress noise and to force a sparse jump function approximation. Note that (d) is significantly more sparse than (c). For this and all other experiments in this paper  $\lambda = 10^{-6}$  was used.

In traditional temperature imaging the complex image of the heating is subtracted by an image before the heating. If the background phase did not change during the heating procedure then

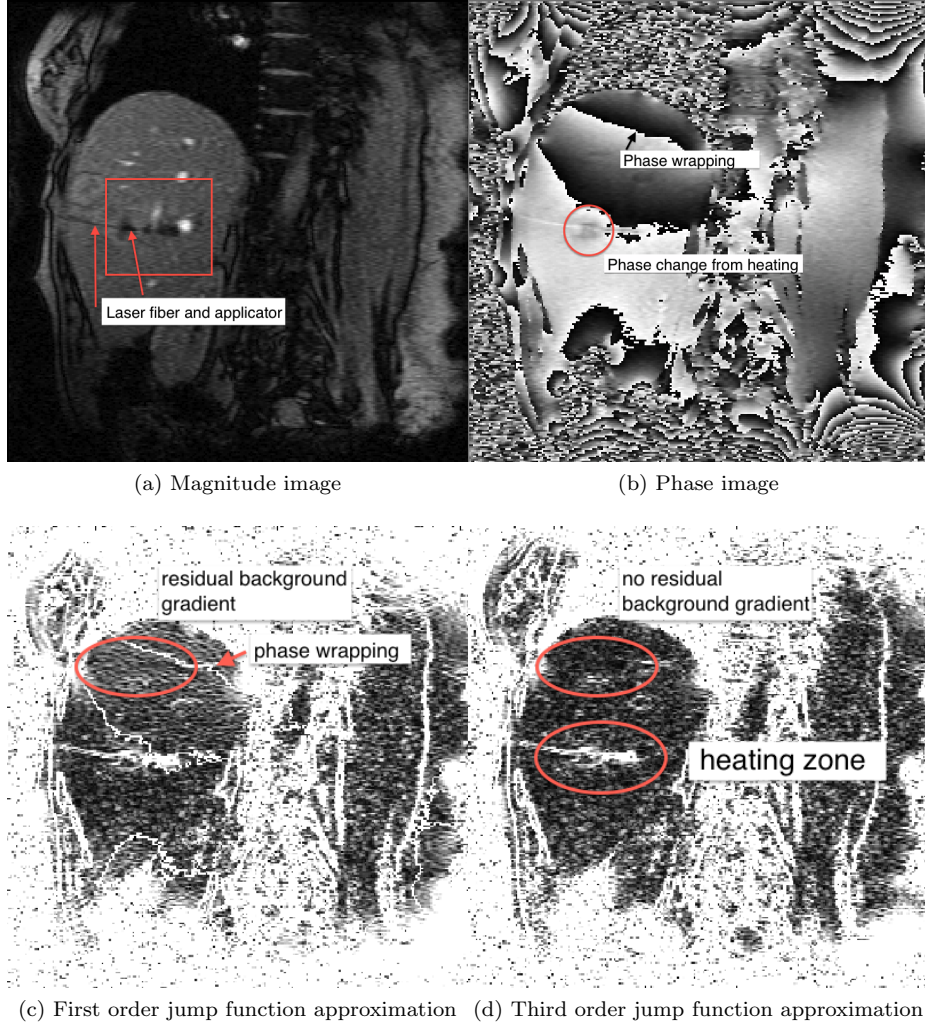


Figure 3: Magnitude and phase of a gradient echo pulse sequence during thermal therapy. The heating causes signal loss in the magnitude image and a shifted phase in the phase image. The phase change due to heating and phase wrapping artifacts are pointed out. The images of Figure 4 are zoomed to the box indicated in (a). Panels (c) and (d) show the magnitude of the jump function of (b) computed using eq. (6) with a first and third order kernel. The first order edge detection clearly shows a residual background shading on the top of the liver, while the third order detector does not show the shading. The phase wrapping jumps in (c) can be easily removed by projecting the jump function to an interval of  $[-\pi, \pi)$ , which was done in (d).

the phase of the resulting image only contains changes due to heating. Thus the procedure is very sensitive to patient motion and other bulk magnetic field changes.

Figure 4 shows a temperature map corresponding to the highlighted region in Figure 3. The left



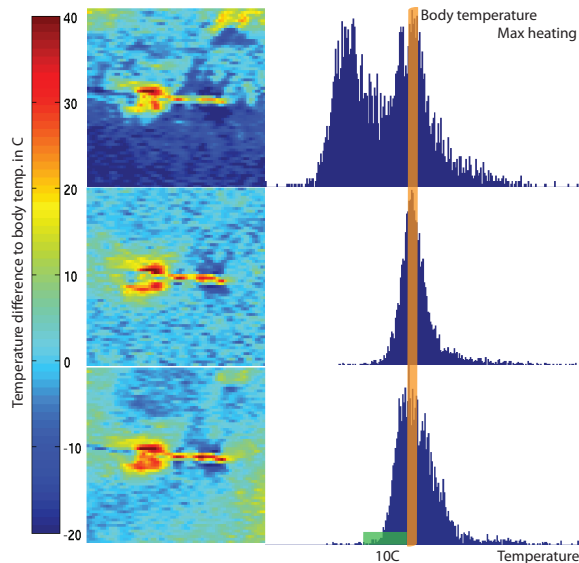


Figure 4: Comparison of reference frame subtraction (top and middle) and the proposed method with patient motion (e.g. due to breathing) between the reference frame and the heating frame. The top and middle rows show a case with and without motion. The bottom row shows the opposed background suppression technique, which does not use a reference frame. The histogram illustrate the temperature distribution in the images relative to the body temperature.

part of the figure shows the temperature image and the right part the histograms corresponding to the images. The temperature maps are obtained using the reference frame subtraction method in the top and middle row and the proposed method in the bottom row. In the top row a pre-heating frame was used, where the background phase changed as compared to the heating frame. Temperature measurements show large variations away from the heating zone in the middle. The temperature histogram on the right also reflects the large variations. The width of the histogram around the body temperature is often used to measure the error of the method. In the the middle row a pre-heating frame was used where the background did not change relative to the heating frame. The histogram on the right is narrower around the body temperature indicating a much smaller measurement error. Unfortunately often it is very difficult or impossible to find a pre-heating frame with the same background phase [29]. The temperature estimate using the proposed method is shown in the bottom row. The temperature map on the left shows a much more homogeneous background, comparable to the top row image. The histogram is also much narrower around the body temperature. This result demonstrates, that our method results in similar temperature estimates as the reference frame subtraction. Of course we cannot expect to obtain exactly the same solution as a successful reference frame subtraction.

Temperature variations around the body temperature are less than 10 degC. The edge detection methods naturally provide the boundary of the laser applicator for this application. Potential difficulties of the proposed method arise if the heating signature is very smooth, or the background contains large gradients. For the proposed method a very smooth temperature change will be absorbed into the background field  $\Phi_b$ . Similarly, large gradients in the background field may be

absorbed into  $\Phi_h$ .

### 3.2 Background Removal for quantitative Susceptibility Weighted Imaging

Figure 5 shows brain data, acquired using a 3T scanner (MR750; GE Healthcare Technologies, Waukesha, WI) from a healthy volunteer, using a 2D-MFGRE sequence with echo spacing = 3.4ms, number of echoes = 16, TE = 2.4 to 28.5 ms, TR = 2200 ms, flip = 60, FOV = 22cm, matrix = 320x256, slice thickness = 5mm, number of slices = 30. An ASSET calibration scan is performed, and sensitivity maps for each of the 32 coils in a 32-channel head coil are obtained. K-space is under-sampled by a factor of 2 by skipping every other frequency encoding line. The magnitude of the first echo is shown in panel (a). The reconstructed images are processed pixel wise by fitting a infinite impulse response (IIR) filter to each echo train. This was done using the Auto Regressive Moving Average (ARMA) [27] technique. The PRF of the dominant peak can be extracted from the coefficients of the IIR filter. The resulting PRF in ppm at each pixel is illustrated in Panel (b). Panel (c) shows the background corrected image. Blood vessels appear darker due to a negative ppm shift of oxidized blood. Brain structures in the mid brain also show significant contrast after applying our background suppression technique. Panel (d) shows the difference of (c) and (b), i.e. the suppressed background. Off resonance shifts can be seen in particular near air cavities near the sinus and the ears. This example demonstrates the potential of the method for quantitative estimation of PRF shifts due to magnetic susceptibility differences for different tissue types.

### 3.3 Noise sensitivity of the background map estimation

In this section we add Gaussian noise of various levels to a chemical shift image with high contrast to noise ratio (CNR) to test the robustness under noise.

An MFGRE sequence was used to collect using a 3T scanner (SIGNA; GE Healthcare Technologies, Waukesha, WI) 16 echoes with echo spacing of 1.816ms, TR = 75ms, Matrix 128 × 128 and Pixel Bandwidth of 651.016Hz. Figure 6 (a) illustrates the magnitude of the first echo of a slice through the pelvis. The multi echo data is processed pixel wise by the ARMA technique. The resulting PRF in ppm at each pixel is illustrated in Panel (b). The dark areas in panel (b) are subcutaneous lipid. Inhomogeneities of the PRF can be seen near the air inclusion in the middle and throughout the image, in particular in the lipid regions. The result of the background suppression technique is shown in Panel (c), which illustrates, that most of the background inhomogeneities have been removed. Note the fat-water ppm difference is about 1.16ppm and not the expected shift of about 3 – 3.5ppm. This is a consequence of aliasing introduced by the finite sampling in echo direction. If the aliasing is taken into account by adding the bandwidth of 4.3212ppm, then the fat-water shift is 3ppm as expected. The pixel wise difference of the images in Panels (b) and (c) is shown in Panel (d). Note that the estimated background field  $\Phi_b$  is smooth in areas of transitions of fat and water. The map is not necessarily smooth in areas of low signal, however a correct estimation of the background in low signal areas is not a well-posed problem.

Noise is added to the original ppm map and a contrast to noise ratio is computed as follows: Two regions of interest (ROIs) are selected  $R_w, R_f$ , one in water the other in fat, labeled 1 and 2 in Figure 6 (c). The size of the ROI is 11 × 11 pixels. The CNR is computed as

$$CNR = \frac{\text{mean}(R_w) - \text{mean}(R_f)}{\text{std}(R_w \cup R_f)}.$$

Figure 7 shows the CNR computed for different noise levels. For very low noise levels the CNR for the uncorrected ppm map is about 60, for the corrected map over 170. This is because the inhomogeneities in the ROIs cause a large standard deviation thus a small CNR for the uncorrected image. With increasing noise the edge detection becomes more difficult and the background suppression method results in lower CNR gains. However the method does not amplify the noise and gives an significant CNR improvement for low and moderate noise levels.

## 4 Conclusion

We have presented a novel background suppression method for MRI phase data. The method works in two stages. First edges are detected in the original phase image using a higher order edge detection method that is based on compressed sensing principles and thus promotes a sparse edge map. In a second stage the corrected phase map is computed by finding a piecewise harmonic function that fits the edges.

We have demonstrated in numerical experiments that the method can be used to remove the background inhomogeneities of gradient echo MRI sequences. Applications include MR temperature imaging and chemical shift imaging. The method is computationally efficient and can remove the background of a  $256 \times 256$  image a few seconds using our non-optimized MATLAB code.

In future work we want to explore other application where inhomogeneities have to be removed and optimize our code. We also would like to improve the performance of the method in regions of very large but smooth gradients in particular near tissue air interfaces.

## Acknowledgment

This research is supported in part by the MD Anderson Cancer Center Support Grant CA016672 and the National Institutes of Health (NIH) award 1R21EB010196-01 and Apache Corporation.

The authors would like to thank Wotao Yin at UCLA for many useful discussions while he was the Post-doc advisor for the first author.

## Acknowledgment

This research is supported in part by the MD Anderson Cancer Center Support Grant CA016672 and the National Institutes of Health (NIH) award 1R21EB010196-01 and Apache Corporation.

The authors would like to thank Wotao Yin at UCLA for many useful discussions while he was the Post-doc advisor for the first author.

## A Detection guarantees

Because the proposed method is based on convex optimization in the context of compressive sensing, we can derive some results when such an edge detection procedure can be expected to be successful.

For simplicity we first consider the one dimensional case, with edge detection kernels of the form (2) with no noise. In this case (6) can be simplified, and renormalized, such that

$$\mathbf{y} = \arg \min_{\mathbf{u}} \left\{ \frac{1}{2} \|\mathbf{u} * \mathbf{w} - \mathbf{c} * \Phi\|_2^2 + \lambda \|\mathbf{u}\|_1 \right\} \quad (8)$$

$$= \arg \min_{\mathbf{u}} \left\{ \frac{1}{2} \|W\mathbf{u} - \mathbf{b}\|_2^2 + \lambda \|\mathbf{u}\|_1 \right\} \quad (9)$$

$$= \arg \min_{\mathbf{u}} \left\{ \frac{1}{2} \left\| \frac{1}{\|\mathbf{c}\|_2} W\mathbf{u} - \frac{\mathbf{b}}{\|\mathbf{c}\|_2} \right\|_2^2 + \frac{\lambda}{\|\mathbf{c}\|_2} \|\mathbf{u}\|_1 \right\}, \quad (10)$$

where  $W$  is the unique Toeplitz matrix such that  $W\mathbf{x} = \mathbf{x} * \mathbf{w}$  for an arbitrary vector  $\mathbf{x}$ . Furthermore,  $\mathbf{b} = \mathbf{c} * \Phi = L\Phi$  and  $L$  is a Toeplitz matrix such that  $L\mathbf{x} = \mathbf{c} * \mathbf{x}$  for arbitrary  $\mathbf{x}$ . The entries of  $\mathbf{c}$  are given by (4) and the entries of  $\mathbf{w}$  by (5).

A key concept to derived reconstruction guarantees in compressive sensing is the concept of the restricted isometry property (RIP). A matrix  $A$  has the RIP if, for an arbitrary choice of an index set  $\mathbf{t}$  with cardinality less or equal to the sparseness  $S$  of the true solution (in other words  $|\mathbf{t}| \leq S$ ), there exists a constant  $\delta_S$ , such that

$$(1 - \delta_S) \|\mathbf{x}\|_2^2 \leq \|A_{\mathbf{t}}\mathbf{x}\|_2^2 \leq (1 + \delta_S) \|\mathbf{x}\|_2^2, \quad (11)$$

for an arbitrary vector  $\mathbf{x}$ . Here  $A_{\mathbf{t}}$  denotes the sub-matrix of  $A$ , obtained by extracting the columns corresponding to the indices in  $\mathbf{t}$ , see e.g. [30].

It is difficult to derive the RIP for an arbitrary selection of columns of  $W$ , however with reasonable restrictions we can derive the following result.

**Theorem 1** *The convolution matrix  $\frac{1}{\|\mathbf{c}\|_2} W$  in (10) has the RIP under the assumption that any two jumps are at least  $m$  points apart.*

**Proof** Any sub-matrix  $W_{\mathbf{t}}$  for  $\mathbf{t}$  such that the indices are at least  $m$  points apart has at most one non-zero entry in each row. In other words the non-zero entries in one column do not overlap with non-zero entries of a different column. Therefore  $\frac{1}{\|\mathbf{c}\|_2^2} W_{\mathbf{t}}^H W_{\mathbf{t}} = I$ , where  $I$  is the identity matrix and  $\left\| \frac{1}{\|\mathbf{c}\|_2} W_{\mathbf{t}} \mathbf{x} \right\|_2^2 = \frac{1}{\|\mathbf{c}\|_2^2} (W_{\mathbf{t}} \mathbf{x})^T (W_{\mathbf{t}} \mathbf{x}) = \frac{1}{\|\mathbf{c}\|_2^2} \mathbf{x}^H W_{\mathbf{t}}^H W_{\mathbf{t}} \mathbf{x} = \|\mathbf{x}\|_2^2$ . And thus, the RIP holds with  $\delta_S = 0$ .

It is proven in [30] that the solution  $\mathbf{y}$  of a convex optimization problem of the form (10), with  $W$  satisfying the RIP, satisfies

$$\|\mathbf{y} - \mathbf{y}^{\#}\|_2 \leq C_{1p} \|W\mathbf{y}^{\#} - \mathbf{b}\|_2 = C_{1p} \|\mathbf{e}\|_2, \quad (12)$$

for a constant  $C_{1p}$  that depends only on  $\delta_S$ . In other words the error that is introduced into  $\mathbf{b}$ , i.e. in our case due to the proposed assumption  $\mathbf{g} \approx \mathbf{w} * \mathbf{u}$ , is at most amplified by a constant, for an appropriate choice of the regularization parameter  $\lambda$ . With  $\delta_S = 0$ ,  $C_{1p} \approx 5.5$ .

**Theorem 2** *For a given order  $m$ , let  $f$  be a piecewise smooth function with  $k$  continuous derivatives in intervals where  $f$  is smooth, sampled on  $N$  equally spaced points, with jumps at least  $m$  points apart. Then, for an appropriate choice  $\lambda$ , there exists a constant  $C$  that depends on  $m$  and the size of the derivatives of  $f$ , such that the error made by solving (10) is bound by*

$$\|\mathbf{y}^{\#} - \mathbf{y}\|_2 \leq \frac{\sqrt{N}}{N^{k_m}} C, \quad (13)$$

where  $k_m = \min(k, m)$ .

**Note:**

Before we prove the theorem, we provide an interpretation of this result: In particular we note that (10) recovers the edges exactly as  $N \rightarrow \infty$ . The theorem also states that the rate of convergence to the true jump function depends on the order of the edge detector  $m$  and the differentiability of  $f$ . The choice of  $\lambda$  is unfortunately not trivial, [30], and depends on the underlying function  $f$  and the order of the edge detector [23, 25]. We also note that the provided error bound in this theorem is a bound on the global error. In practice the error varies locally. In particular numerical results show that the local error is typically very small away from jumps and larger at jumps. The local nature of the error is not captured by the stated theorem. Our numerical experiments show also, that the local error is bounded even if jumps are closer than  $m$  points. However, it is larger than the error at the jump if jumps are separated by at least  $m$  points. Overall the theorem provides an convergence guarantee, but is not a very *sharp* result.

**Proof** The model error introduced by the assumption  $L\Phi \approx W\mathbf{y}^\#$  is given by

$$\mathbf{e} = L\Phi - W\mathbf{y}^\#.$$

From the definition of  $\mathbf{w}$  in (5) it follows that the error is zero for piecewise constant functions. Thus, we decompose  $\Phi$  in a sum of a piecewise constant and a smooth part near the jumps. Let  $J$  be the original domain of  $f$ , and let  $J_1, \dots, J_n$  be a partition of  $J$ , such that each sub-interval  $J_i$  contains the jump at location  $\xi_i$ . We further require  $\bigcup J_i = J$  and  $\bigcap J_i = \emptyset$ . Let  $f_1(x), \dots, f_n(x)$  be functions defined on the whole real line, such that  $f(x) = f_i(x)$  for  $x \in J_i$  and  $f_i(x) \in C^k$  for all  $x \neq \xi_i$ . Let

$$\begin{aligned} H(x) &= \begin{cases} 0 & \text{for } x < 0 \\ 1 & \text{for } x \geq 0 \end{cases}, \\ s_i(x) &:= [f](\xi_i)H(x - \xi_i), \end{aligned}$$

and  $r_i(x) = f_i(x) - s_i(x) \in C^k$ . Here,  $k$  is the largest number such that  $r_i$  and  $f_i$  exist. Let  $\mathbf{s}_i$ ,  $\mathbf{r}_i$  and  $\Phi_i$  be vectors with point evaluations of  $s_i(x)$ ,  $r_i(x)$  and  $f_i(x)$  respectively. Then, we see that

$$\mathbf{e}_i = L\Phi_i - W\mathbf{y}_i^\# = L(\mathbf{s}_i + \mathbf{r}_i) - W\mathbf{y}_i^\# = L\mathbf{r}_i.$$

In other words the error in each subinterval can be estimated by the error that is made by applying the edge detector to a function that is at least continuous. It is shown in e.g. [24], that the point wise error made by the finite difference edge detector away from jumps can be bound by:

$$\|L\mathbf{r}_i\|_\infty \leq \tilde{C}_i h^{k_m}, \tag{14}$$

where  $h$  is the grid spacing,  $k_m = \min(k, m)$  and  $\|\cdot\|_\infty$ , i.e. the maximum absolute value of a vector.  $\tilde{C}_i$  is a constant that only depends on the order  $m$  of the edge detector. Let  $\mathbf{1}$  be a the vectors with entries 1, then with

$$\|x\|_2 \leq \|\mathbf{1}\|_2 \|x\|_\infty = \sqrt{N} \|x\|_\infty,$$

we can bound the  $l_2$  error of the edge detection by  $\|\mathbf{e}\|_2 \leq \tilde{C} \frac{\sqrt{N}}{N^{k_m}}$ . Combining this result with (12) yields:

$$\|y - y^\#\|_2 \leq \frac{\sqrt{N}}{N^{k_m}} C.$$

## References

- [1] F. Schweser, B. Lehr, A. Deistung, and J. Reichenbach, "A novel approach for separation of background phase in swi phase data utilizing the harmonic function mean value property," *Stockholm, Sweden: ISMRM*, p. 142, 2010.
- [2] D. Fuentes, J. Yung, J. D. Hazle, J. S. Weinberg, and R. J. Stafford, "Kalman Filtered MR Temperature Imaging for Laser Induced Thermal Therapies," *Trans. Medical Imaging*, vol. 31, no. 4, pp. 984–994, 2012.
- [3] S. Wharton, A. Schäfer, and R. Bowtell, "Susceptibility mapping in the human brain using threshold-based k-space division," *Magnetic Resonance in Medicine*, vol. 63, no. 5, pp. 1292–1304, 2010. [Online]. Available: <http://onlinelibrary.wiley.com/doi/10.1002/mrm.22334/full>
- [4] A. Rauscher, J. Sedlacik, M. Barth, H. J. Mentzel, and J. R. Reichenbach, "Magnetic susceptibility-weighted mr phase imaging of the human brain," *AJNR*, no. 26, pp. 736–742, 2005.
- [5] J. H. Duyn, P. v. Gelderen, T. Li, J. A. d. Zwart, A. P. Koretsky, and M. Fukunaga, "High-field mri of brain cortical substructure based on signal phase," *PNAS*, vol. 28, no. 104, pp. 11 796–11 801, June 2007.
- [6] E. M. Haacke, Y. Xu, Y.-C. N. Cheng, and J. R. Reichenbach, "Susceptibility weighted imaging (swi)," *Magnetic Resonance in Medicine*, vol. 52, no. 3, pp. 612–618, 2004. [Online]. Available: <http://onlinelibrary.wiley.com/doi/10.1002/mrm.20198/full>
- [7] E. M. Haacke and J. R. Reichenbach, Eds., *Susceptibility Weighted Imaging in MRI: Basic Concepts and Clinical Applications*. Wiley-Blackwell, 2011, vol. 1.
- [8] L. de Rochefort, R. Brown, M. R. Prince, and Y. Wang, "Quantitative mr susceptibility mapping using piece-wise constant regularized inversion of the magnetic field," *Magnetic Resonance in Medicine*, vol. 60, no. 4, pp. 1003–1009, 2008. [Online]. Available: <http://onlinelibrary.wiley.com/doi/10.1002/mrm.21710/full>
- [9] D. Zhou, T. Liu, P. Spincemaille, and Y. Wang, "Background field removal by solving the Laplacian boundary value problem." *NMR in biomedicine*, vol. 27, no. 3, pp. 312–9, Mar. 2014.
- [10] T. Liu, P. Spincemaille, L. de Rochefort, B. Kressler, and Y. Wang, "Calculation of susceptibility through multiple orientation sampling (cosmos): a method for conditioning the inverse problem from measured magnetic field map to susceptibility source image in mri," *Magnetic Resonance in Medicine*, vol. 61, no. 1, pp. 196–204, 2009. [Online]. Available: <http://onlinelibrary.wiley.com/doi/10.1002/mrm.21828/full>
- [11] J. Neelavalli, Y.-C. N. Cheng, J. Jiang, and E. M. Haacke, "Removing background phase variations in susceptibility-weighted imaging using a fast, forward-field calculation," *Journal of Magnetic Resonance Imaging*, vol. 29, no. 4, pp. 937–948, 2009. [Online]. Available: <http://onlinelibrary.wiley.com/doi/10.1002/jmri.21693/full>

- [12] K. M. Koch, X. Papademetris, D. L. Rothman, and R. A. de Graaf, “Rapid calculations of susceptibility-induced magnetostatic field perturbations for in vivo magnetic resonance,” *Physics in medicine and biology*, vol. 51, no. 24, p. 6381, 2006. [Online]. Available: <http://iopscience.iop.org/0031-9155/51/24/007>
- [13] M. C. Langham, J. F. Magland, T. F. Floyd, and F. W. Wehrli, “Retrospective correction for induced magnetic field inhomogeneity in measurements of large-vessel hemoglobin oxygen saturation by mr susceptometry,” *Magnetic Resonance in Medicine*, vol. 61, no. 3, pp. 626–633, 2009. [Online]. Available: <http://onlinelibrary.wiley.com/doi/10.1002/mrm.21499/full>
- [14] Y. Wang, Y. Yu, D. Li, K. Bae, J. Brown, W. Lin, and E. Haacke, “Artery and vein separation using susceptibility-dependent phase in contrast-enhanced mra,” *Journal of Magnetic Resonance Imaging*, vol. 12, no. 5, pp. 661–670, 2000.
- [15] B. Yao, T.-Q. Li, P. v. Gelderen, K. Shmueli, J. A. de Zwart, and J. H. Duyn, “Susceptibility contrast in high field mri of human brain as a function of tissue iron content,” *Neuroimage*, vol. 44, no. 4, pp. 1259–1266, 2009. [Online]. Available: <http://www.sciencedirect.com/science/article/pii/S1053811908011191>
- [16] W. A. Grissom, M. Lustig, A. Holbrook, V. Rieke, J. M. Pauly, and K. Butts-Pauly, “Reweighted 1 referenceless prf shift thermometry,” *Magnetic Resonance in Medicine*, vol. 64, no. 4, pp. 1068–1077, October 2010.
- [17] R. Salomir, M. Viallon, A. Kickhefel, J. Roland, D. R. Morel, L. Petrusca, V. Auboiroux, T. Goget, S. Terraz, C. D. Becker, and P. Gross, “Reference-free prfs mr-thermometry using near-harmonic 2-d reconstruction of the background phase,” *IEEE Trans Med Imaging*, vol. 31, no. 2, pp. 287–301, Feb 2012.
- [18] W. Li, A. V. Avram, B. Wu, X. Xiao, and C. Liu, “Integrated laplacian-based phase unwrapping and background phase removal for quantitative susceptibility mapping,” *NMR in Biomedicine*, vol. 27, no. 2, pp. 219–227, 2014, nBM-13-0182.R2. [Online]. Available: <http://dx.doi.org/10.1002/nbm.3056>
- [19] J. Canny, “A computational approach to edge detection,” *IEEE Trans. Pattern Anal. Mach. Intell.*, vol. 8, no. 6, pp. 679–698, 1986.
- [20] S. Mallat and S. Zhong, “Characterization of signals from multiscale edges,” *IEEE Trans. Pattern Anal. Mach. Intell.*, vol. 14, no. 7, pp. 710–732, 1992.
- [21] A. Gelb and E. Tadmor, “Adaptive Edge Detectors for Piecewise Smooth Data Based on the minmod Limiter,” *Journal of Scientific Computing*, vol. 28, no. 2-3, pp. 279–306, Sep. 2006. [Online]. Available: <http://www.cscamm.umd.edu/people/faculty/tadmor/pub/spectral-approximations/Gelb-Tadmor.JSC2006.pdf>
- [22] M. Lustig, D. Donoho, and J. M. Pauly, “Sparse mri: The application of compressed sensing for rapid mr imaging,” *Magn Reson Med*, vol. 58, no. 6, pp. 1182–95, Dec 2007.
- [23] W. Stefan, A. Viswanathan, A. Gelb, and R. Renaut, “Sparsity enforcing edge detection method for blurred and noisy fourier data,” *Journal of Scientific Computing*, vol. 50, no. 3, pp. 536–556, 2012.

- [24] R. Archibald, A. Gelb, and J. Yoon, "Polynomial Fitting for Edge Detection in Irregularly Sampled Signals and Images," *SIAM Journal on Numerical Analysis*, vol. 43, no. 1, pp. 259–279, 2005.
- [25] W. Stefan, R. A. Renaut, and A. Gelb, "Improved total variation-type regularization using higher-order edge detectors," *In preparation*, 2008.
- [26] C. Wu and X.-C. Tai, "Augmented lagrangian method, dual methods, and split bregman iteration for rof, vectorial tv, and high order models," *SIAM J. Imaging Sciences*, vol. 3, no. 3, pp. 300–339, 2010.
- [27] B. A. Taylor, K. P. Hwang, A. M. Elliott, A. Shetty, J. D. Hazle, and R. J. Stafford, "Dynamic chemical shift imaging for image-guided thermal therapy: analysis of feasibility and potential," *Med Phys*, vol. 35, no. 2, pp. 793–803, Feb 2008. [Online]. Available: <http://www.hubmed.org/display.cgi?uids=18383702>
- [28] R. Saxena, A. Gelb, and H. D. Mittelmann, "A High Order Method for Determining the Edges in the Gradient of a Function," *Communications in Computational Physics*, vol. 5, no. 2-4, pp. 694–711, 2009.
- [29] K. K. Vigen, B. L. Daniel, J. M. Pauly, and K. Butts, "Triggered, navigated, multi-baseline method for proton resonance frequency temperature mapping with respiratory motion," *Magn Reson Med*, vol. 50, no. 5, pp. 1003–10, Nov 2003.
- [30] E. J. Candès and T. Tao, "Near-optimal signal recovery from random projections: Universal encoding strategies?" *IEEE Transactions on Information Theory*, vol. 52, no. 12, pp. 5406–5425, 2006.



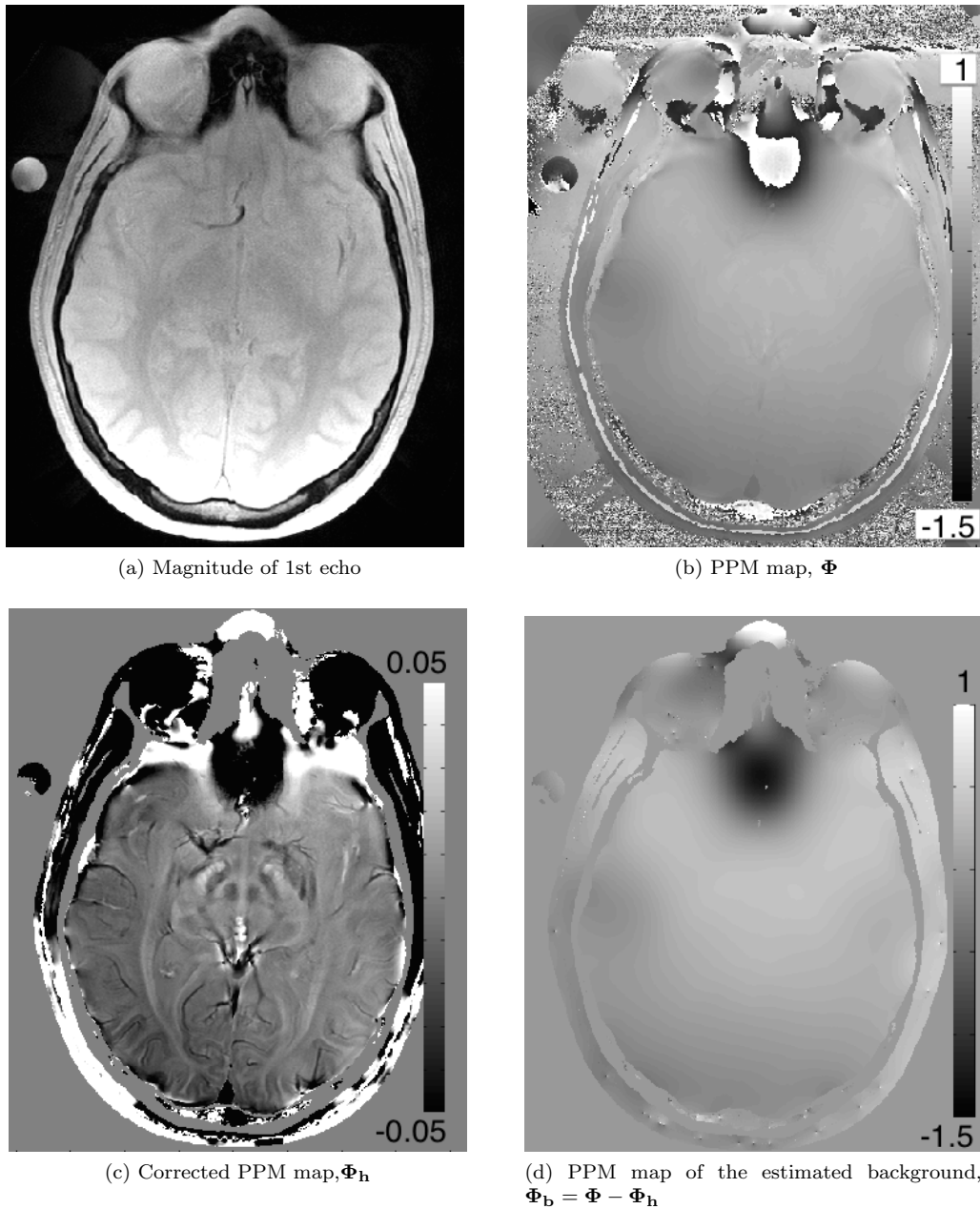


Figure 5: Background suppression of a ppm map in a healthy volunteer. (a): Magnitude of the first echo of a multi echo sequence. (b): PRF map estimation using ARMA technique.(c): Background suppressed PRF map. Blood vessels appear darker due to magnetic susceptibility effects. (d): Estimated background field map in ppm.

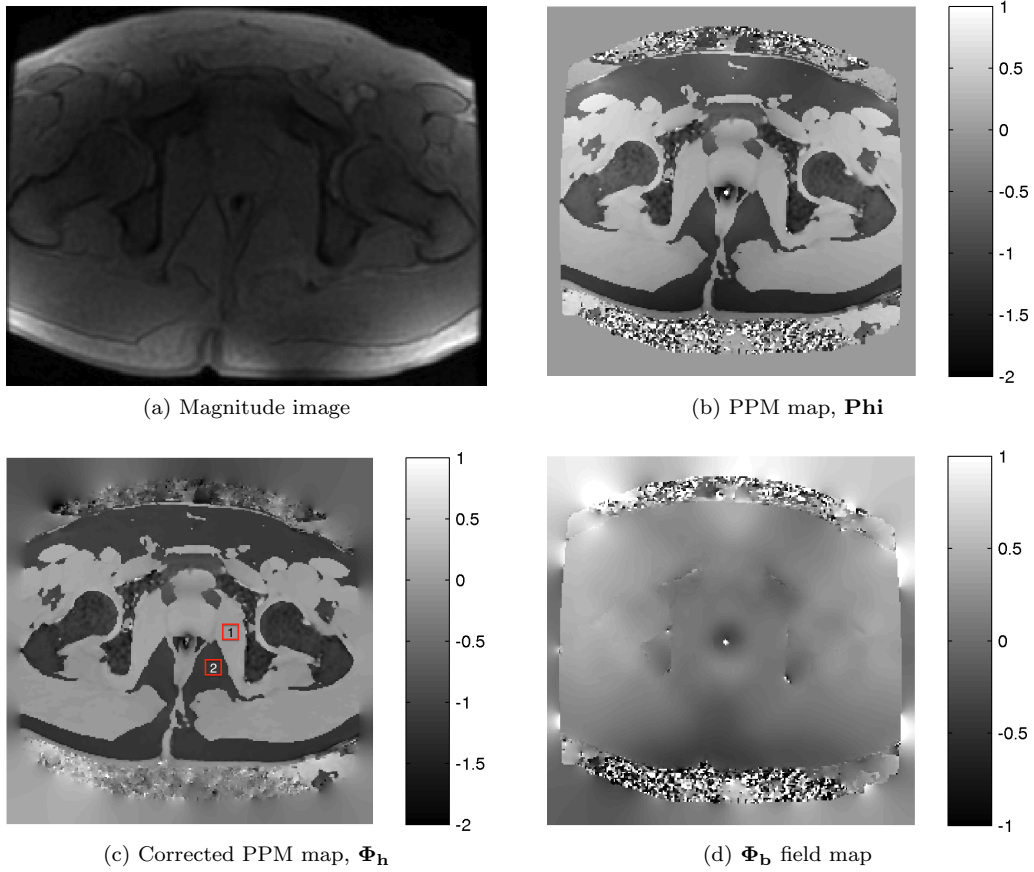


Figure 6: Background suppression of a ppm map with water and fat signal. (a): Magnitude of the first echo of a multi echo sequence. (b): PRF map estimation using ARMA technique.(c): Background suppressed PRF map. (d): Estimated background field map in ppm. The fat and water peak is aliased with 4.32 ppm due to the chosen echo spacing. the fat-water boundary. The labels 1 and 2 are water and fat ROIs that are used to determine the CNR gain of the method.

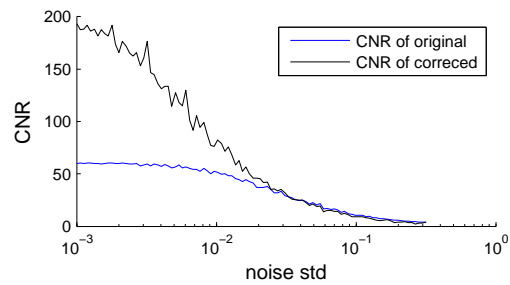


Figure 7: Contrast to noise ratio for different levels of noise is shown. The uncorrected image has a low CNR even at small noise levels because of the inhomogeneity of the background. For larger noise levels the CNR of the background suppression is reduced because the edge detection step becomes less well posed. However, the CNR is on average is larger than the CNR of the original data.